Springer

Journal of
Mechanical
Science and
Technology

Journal of Mechanical Science and Technology 22 (2008) 1684~1691

www.springerlink.com/content/1738-494x
DOI 10.1007/s12206-008-0516-4

Nondestructive evaluation of a crack on austenitic stainless steel using a sheet type induced current and a Hall sensor array

Jongwoo Jun[1] and Jinyi Lee[2,*]

[1]*Department of Information and Communication Engineering, Graduate School, Chosun University, 375 Seosuk-dong, Dong-gu, Gwangju 501-759, Korea*
[2]*Department of Control and Instrumentation Robot Engineering, Chosun University, 375, Seosuk-dong, Dong-gu, Gwangju 501-759, Korea*

(Manuscript Received November 5, 2007; Revised May 1, 2008; Accepted May 14, 2008)

Abstract

Austenitic stainless steels (hereafter A-STS) such as STS304 and STS316 are paramagnetic metals. However, a small amount of partial magnetization is generated in A-STS because of the imperfect final heat treatment and mechanical processing. Surface cracks on paramagnetic metal with a partially magnetized region (hereafter PMR) are difficult to inspect. In this paper, we propose a method for high speed inspection and evaluation of a crack on A-STS. Cracks can be inspected with high speed by using 64 arrayed Hall sensors (HSA) with 3.5 mm spatial resolution and a sheet type induced current (STIC). Then, a crack can be evaluated quantitatively by using the detailed distribution of the magnetic field obtained by using single Hall sensor scanning (SSS) around the inspected crack area. Several cracks on A-STS with partially magnetized areas were examined and the experimental formulas were derived.

Keywords: Nondestructive evaluation; Sheet type induced current; Austenitic stainless steel; Sensor array; Sensor scanning

1. Introduction

Austenitic stainless steels (hereafter A-STS) such as SUS304 and SUS316 have been used in important mechanical structures with very large sizes, such as nuclear power plants, chemical plants, food industry facilities, and petrol storage tanks, because of their excellent anti-corrosive and heat resistant properties. The cracks on these mechanical structures have to be rapidly inspected and evaluated quantitatively in damage tolerance engineering [1, 2]. Usually, a nondestructive inspection method is correspondent with material properties. A-STS are paramagnetic metals where eddy current testing is useful. But, a small amount of partial magnetization is generated in A-STS because of their imperfect final heat treatments and mechanical processing such as rolling and welding. Correspondingly, the partially magnetized region (hereafter PMR) may be misrecognized as a crack when using previous types of nondestructive testing.

Conversely, the real time inspection of a crack in a large area (e.g., a circle area with a diameter of 75 mm) at a high spatial resolution is an advantage of MOI (magneto-optical/eddy current imaging) [3, 4], [5]. MOI was developed for use in inspecting fatigue cracks and corrosion in aluminum alloys of aged aircraft. We induced a sheet type current on the specimen to generate a magnetic flux around a crack in the MOI. A sheet type induced current (STIC) is distorted when there is a crack. This distorted current induces a magnetic flux in a direction normal to the specimen. Therefore, the crack can be detected by using magnetic optical film (MO film) and a polarized optical system. However, the magnetic domains of the MO film of the MOI, having small saturated magnetization (H_S), are saturated partially on A-STS because of the external magnetic field (H_{EXT}) of the PMR ex-

*Corresponding author. Tel.: +82 62 230 7101, Fax.: +82 62 230 6858
E-mail address: jinyilee@chosun.ac.kr

ceeds H_S. Therefore, the surface cracks on partially magnetized A-STS are difficult to inspect by using MOI. Also, the shape and depth of the cracks are difficult to evaluate quantitatively because the distribution of the magnetic field cannot be obtained by MOI.

A magnetic camera using Hall sensors has been developed to inspect and evaluate cracks [6-9]. The distribution of the magnetic field can be measured quantitatively; then, the crack can be evaluated with a scan type magnetic camera [10]. On the other hand, a type of area magnetic camera using a Hall sensor array (HSA) has merit; that is, a crack can be detected with high speed without sensor scanning. However, the spatial resolution of an HSA is low so the detailed distribution of a magnetic field cannot be obtained. The detailed distribution of the magnetic field can be obtained by using single sensor scanning (hereafter SSS). But a large scanning time is necessary in SSS.

In this paper, we propose high speed improved nondestructive testing and evaluating method. An STIC is induced on the A-STS, having a PMR and distortion around the tip of a crack. As a result, the alternating magnetic field, which is due to the crack existence, with a bias magnetic field due to the existence of the PMR, is produced. We propose a signal processing circuit for measuring the root-mean-square value (RMS) of the alternating magnetic field without the bias magnetic field. The distribution of the magnetic field with low spatial resolution can be visualized by using an HSA in real time. The detailed magnetic field distribution around a detected crack area is obtained by using SSS for evaluating the crack. Scanning time can be decreased because the scan area can be limited by using this method. We evaluated the crack length, width, depth, section area, and volume by using experimentally obtained formulas.

2. The principle

An STIC is used to induce a current in a specimen as shown in Fig. 1. The alternating current (AC) input at 2.3 A and 6.4 kHz on the primary coil ((a) in Fig. 1) generates an alternating magnetic flux in the core ((b) in Fig. 1). At the same time, a homogeneous current is induced in the copper sheet ((c) in Fig. 1), which passes through the core. An STIC is induced when the copper sheet is located on the surface of the specimen ((d) in Fig. 1). Also, an eddy current is generated from the existence of a crack because the STIC

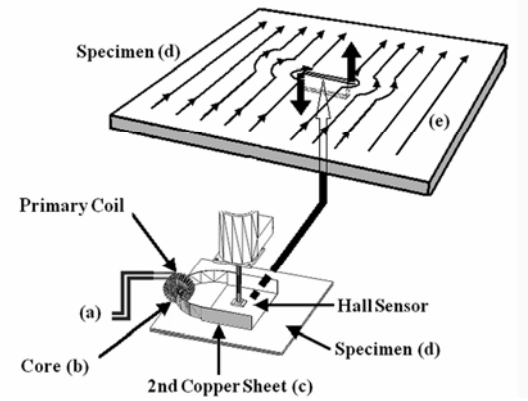

Fig. 1. Schematics of the sheet type induced current (STIC).

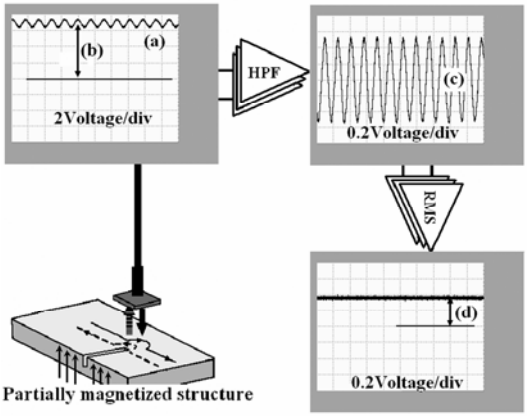

Fig. 2. Extraction of the amplitude of alternating current signal due to crack existence.

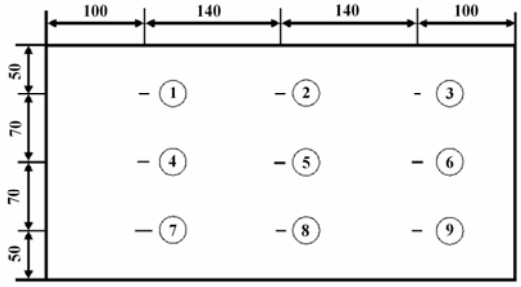

Fig. 3. Geometry of the investigated austenitic stainless steel specimen (Unit: mm, Thickness: 10 mm).

on the specimen is distorted at both tips of the crack. Correspondingly, a magnetic field is generated around a crack as shown (e) in Fig. 1.

The frequencies of each output of the Hall sensor coincide with the frequency of the input current of the primary coil as shown (a) in Fig. 2. Also, the bias

output is mixed with the alternative Hall voltage, as shown (b) in Fig. 2, because the specimen contains a PMR in the A-STS. The amplitude of the alternating Hall voltage ((c) in Fig. 2) can be converted to the direct response signal ((d) in Fig. 3) by using a high-pass-filter (HPF) and the root-mean-squared (RMS) circuit ignoring the bias voltage.

3. Experiments and discussion

3.1 The specimens and experimental equipment

Cracks (9 slits) were introduced on partially magnetized A-STS, a SUS304 specimen, by using electronic discharge machining as shown in Fig. 3. Table 1 shows the dimensions of each crack. Fig. 4 shows a result of crack observation by using MOI. The crack was difficult to inspect by using MOI because of the PMR in the A-STS.

Table 1. Dimensions of each crack on the austenitic stainless steel specimen.

Crack No.	Depth (mm)	Width (mm)	Length (mm)
1	2	0.79	10
2	4	0.82	10
3	6	0.82	5
4	6	0.61	10
5	6	0.80	10
6	6	0.98	10
7	6	0.74	15
8	8	0.80	10
9	9	0.80	10

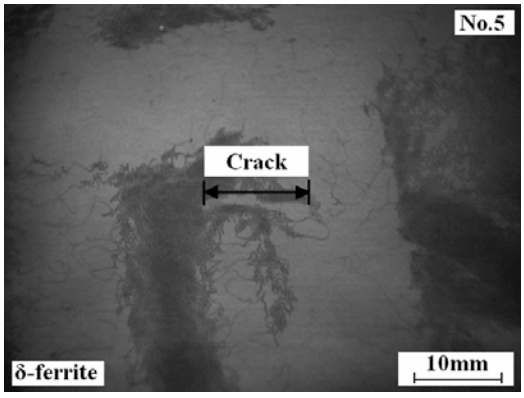

Fig. 4. Detection result of crack No.5 at 6.4 kHz by using MOI 308/3 (Produced by PRI).

The 64 Hall sensors of the HSA were arrayed in an 8 by 8 configuration of 3.5 mm spatial resolution as shown in Fig. 5. Therefore, the crack in the 28 mm by 28 mm area can be detected at the same time in this structure. The HSA was positioned on a copper sheet which induced STIC on a specimen. The AC input at 2.3 A and 6.4 kHz was derived from a function generator and amplified by an AC power amplifier. The AC input was applied to the primary coil and it generated the STIC on the copper sheet. There were 45 and 46 turns of the primary coils in the HSA and SSS, respectively. Also, the thickness and the area of the copper sheet were 100×105 mm by 0.3 mm and 150×110 mm by 0.4 mm in the HSA and SSS, respectively. The copper sheet was positioned on the specimen. The lift-offs were 0.5 mm and 1 mm in the HSA and SSS, respectively.

3.2 Real time inspection of the crack by using an HSA

A HSA (Fig. 5) was used to confirm the real time inspection. The distribution of RMS Hall voltages, using a MX636JN RMS to DC converter, was obtained from a HSA of 3.5 mm spatial resolution (hereafter $DRMS_{LOW}$).

The $DRMS_{LOW}$ permitted crack detection of the partially magnetized specimen in real time. Two peak values from the $DRMS_{LOW}$ appeared at both tips of the crack, as shown in Fig. 6, because the STIC was distorted at the tips of the crack and the magnetic field was maximized at the same position. Also, the height of the peak was closely related to the crack size.

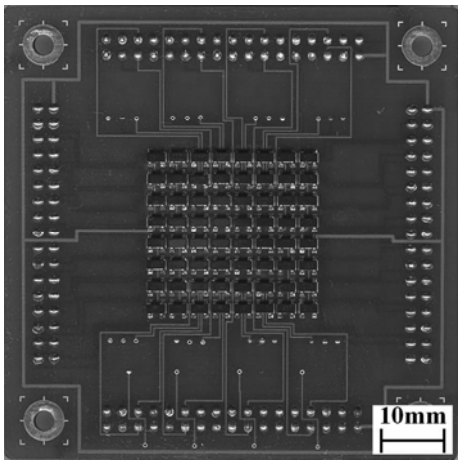

Fig. 5. A photograph of the Hall sensor array (HSA).

However, the $DRMS_{LOW}$ was difficult to use in evaluating a crack because of its low spatial resolution.

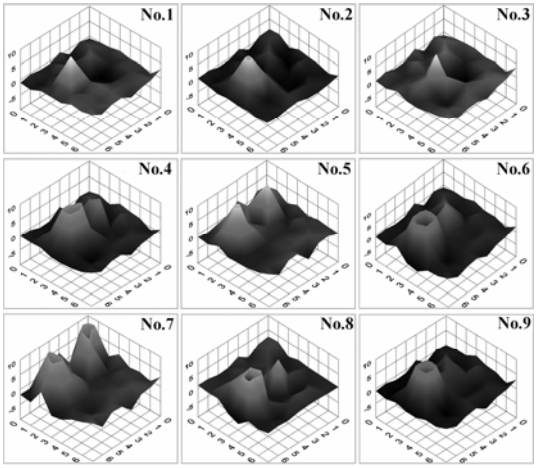

Fig. 6. Experimental results using hall sensor array (HSA).

3.3 Evaluation of the crack using SSS

The SSS could obtain the distribution of the RMS Hall voltage by using an MX636JN with a large spatial resolution of 0.5 mm (hereafter $DRMS_{HIGH}$). Fig. 7 shows the $DRMS_{HIGH}$ and its differential value in the STIC direction, $\partial(D_{HIGH})/\partial x$. The maximum value of the $DRMS_{HIGH}$ increased according to the depth of the crack (D_C) when the width (W_C) and length (L_C) of the crack were fixed as shown in Fig. 7, No.1, No.2, No.3, No.8, and No.9. These phenomena can be explained by the skin effect and with the help of the detailed Eq. (1). The density of the induced current on the subsurface *Jt* is defined in the following Eq. [11].

$$Jt = e^{-t/\delta} Js \tag{1}$$

where, t and δ are the depth and skin depth, respectively. *Js* denotes the induced current on the surface. Here, the skin depth δ is defined as [12]:

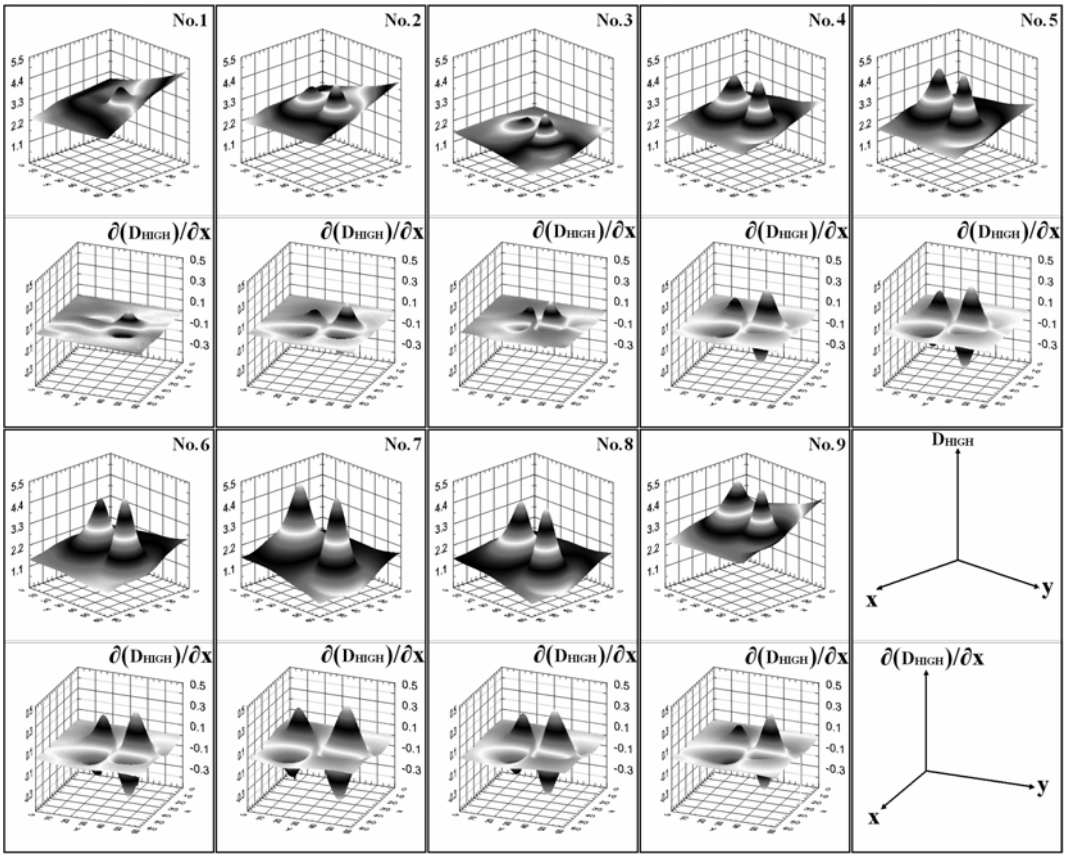

Fig. 7. Distributions of $DRMS_{HIGH}$ and $\partial D_{HIGH}/\partial x$ by using single sensor scanning (SSS).

$$\delta = \frac{1}{\sqrt{\pi f \mu \sigma}} \tag{2}$$

where, f, μ and σ are frequency, permeability, and electrical conductivity, respectively. According to specimen SUS 304, μ and σ were assumed to be 1 and 2, respectively [13]. At a frequency of 6.4 kHz, the skin depth (δ) was 5 mm. Also from Eq. (1), Jt / Js = 37 % if $t = \delta$ (=5 mm). For crack No.9, t = 9 mm, so Jt / Js = 16.5 %. Correspondingly, we could distinguish the deepest crack (9 mm) with other shallow cracks in this STIC experiment.

Fig. 8 shows the meaning of Max[$\partial(D_{HIGH})/\partial x$], Distance[$\partial(D_{HIGH})/\partial x$], and Diameter[$\partial(D_{HIGH})/\partial x$] in the $\partial(D_{HIGH})/\partial x$ distribution. The interval between the maximum position and the minimum position (hereafter, Diameter[$\partial(D_{HIGH})/\partial x$]) in $\partial(D_{HIGH})/\partial x$, which represented the gradient of each peak, was closely related to the crack parameter, Dc. Conversely, the distance between each set of maximum positions (hereafter Distance[$\partial(D_{HIGH})/\partial x$]) showed a close relationship with L_C, as shown in Fig. 7, No. 3, No. 5, and No. 7.

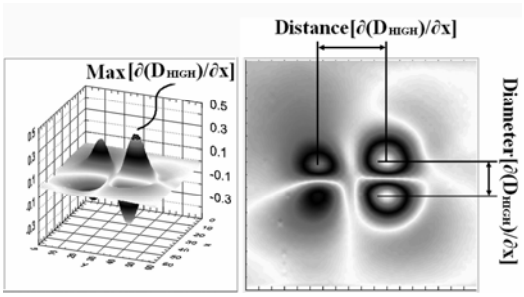

Fig. 8. The meaning of Max[$\partial(D_{HIGH})/\partial x$], Distance[$\partial(D_{HIGH})/\partial x$], and Diameter[$\partial(D_{HIGH})/\partial x$]

Fig. 9 shows the relationship between Max[$\partial(D_{HIGH})/\partial x$], Distance[$\partial(D_{HIGH})/\partial x$], and the crack parameters (D_C, L_C, and W_C). The Max[$\partial(D_{HIGH})/\partial x$] showed a close relationship with D_C as shown in Eq. (3), which was derived from cracks No.1, No.2, No.5, and No.8 in Fig. 9(a) when the W_C and L_C were fixed.

$$Dc = 23.6574 \times Max\left[\partial(D_{HIGH})/\partial x\right] - 0.02765 \tag{3}$$

Also, the Distance[$\partial(D_{HIGH})/\partial x$] showed a close relationship with the L_C as shown in Eq. (4), which was derived from cracks No.3, No.5, and No.7 in Fig. 9(b).

$$Lc = 1.25837 \times Distance\left[\partial(D_{HIGH})/\partial x\right] - 1.89301 \tag{4}$$

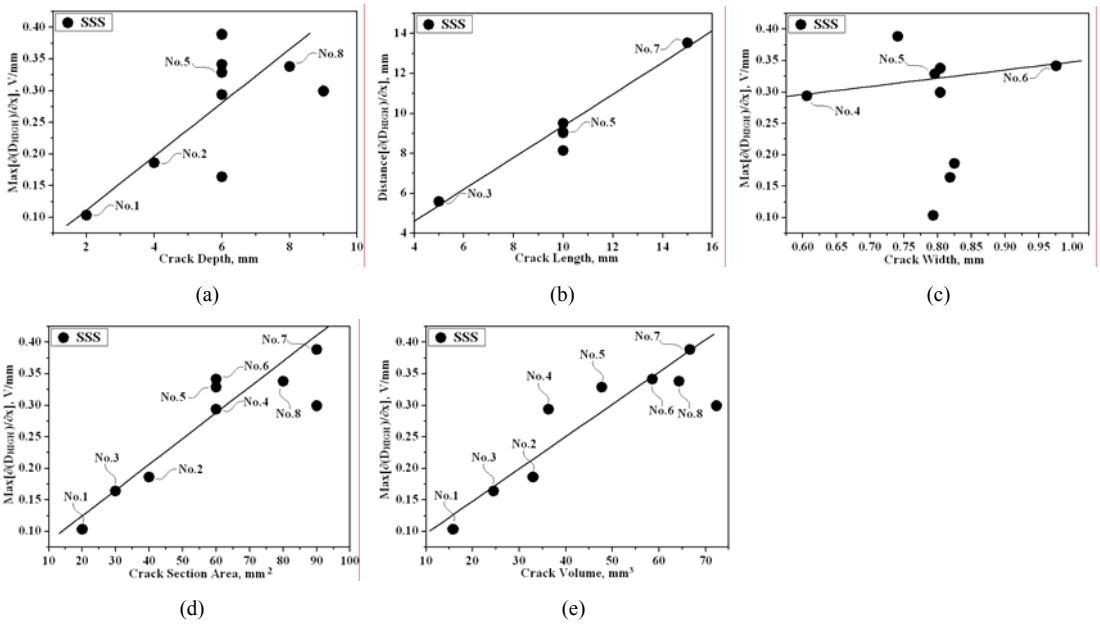

Fig. 9 The relationship between the NDE factors and the crack parameters (D_C, L_C, and W_C).

Furthermore, the Max[$\partial(D_{HIGH})/\partial x$] showed a close relationship W_C as shown in Eq. (5), which was derived from cracks No.4, No.5, and No.6 in Fig. 9(c).

$$Wc = 8.31739 \times Max\left[\partial(D_{HIGH})/\partial x\right] - 1.97097 \quad (5)$$

In addition, the section area, S_C, and the volume of the crack, V_C, can be calculated by using Eq. (6) and Eq. (7), derived from (d) and (e) in Fig. 9, respectively.

$$Sc = 244.49878 \times Max\left[\partial(D_{HIGH})/\partial x\right] - 10.53301 \quad (6)$$

$$Vc = 194.9318 \times Max\left[\partial(D_{HIGH})/\partial x\right] - 8.88109 \quad (7)$$

The L_C, Eq. (4), showed less error than the W_C and D_C equations. Also, the section area Eq. (6), derived from (d) in Fig. 9, showed a small error. Correspondingly, D_C' can be calculated from S_C by using Eq. (8) because the section area is multiplied by L_C and D_C'.

$$Dc' = Sc/Lc = \frac{\{244.49878 \times Max\left[\partial(D_{HIGH})/\partial x\right] - 10.53301\}}{\{1.25837 \times Distance\left[\partial(D_{HIGH})/\partial x\right] - 1.89301\}} \quad (8)$$

We calculated the depth of the crack with extreme accuracy by using Eq. (8) and compared it with Eq. (3) as shown in Fig. 10.

The Max[$\partial(D_{HIGH})/\partial x$] included relevant information on the depth, width, and length of the crack. Also, the changes of depth and length were affected more easily than that of the width. Fortunately, the length of the crack, L_C, could also be calculated by using Distance[$\partial(D_{HIGH})/\partial x$] with less error than W_C and correspondingly, the calculated volume of the crack, obtained by multiplying L_C (Eq. (4)), W_C (Eq. (5)), and D_C' (Eq. (8)), as shown in Eq. (9). We expect this calculation to have less error.

$$Volume = Lc \times Wc \times Dc' \quad (9)$$

However, the calculated volume using Eq. (9), with a bigger error than Eq. (7) at 72mm^3 of volume, was obtained as shown in Fig. 11. The bigger errors resulted from the accumulation of errors in Eq. (4), Eq. (5), and Eq. (8).

4. Conclusions

We proposed a nondestructive evaluation method for cracks occurring on the surface of austenitic stainless steel with a partially magnetized area in real time. The crack was inspected in real time by using a Hall sensor array and a sheet type induced current. And the distribution of the magnetic field ($DRMS_{HIGH}$), the differential value of $DRMS_{HIGH}$ ($\partial(D_{HIGH})/\partial x$), the maximum value of $\partial(D_{HIGH})/\partial x$ (Max[$\partial(D_{HIGH})/\partial x$]), the interval between the maximum position and minimum position in the $\partial(D_{HIGH})/\partial x$ (Diameter[$\partial(D_{HIGH})/\partial x$]), and the distance between each set of maximum positions (Distance[$\partial(D_{HIGH})/\partial x$] were obtained by using single sensor scanning at the inspected crack area.

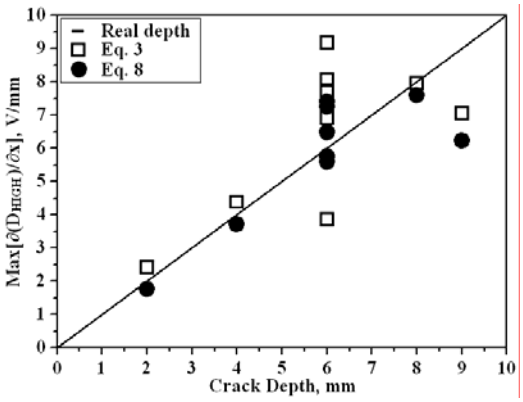

Fig. 10. Comparison of calculated crack depths by using Eq. (3) and Eq. (8).

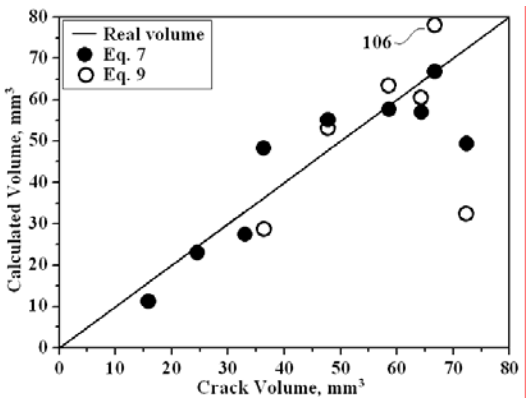

Fig. 11. Comparison of calculated crack volumes by using Eq. (7) and Eq. (9).

The depth, width, length, section area, and volume of the crack, can be calculated by equations derived from the relationship between the Max[$\partial(D_{HIGH})/\partial x$], Distance[$\partial(D_{HIGH})/\partial x$], Diameter[$\partial(D_{HIGH})/\partial x$], and the crack morphologies.

Acknowledgements

This work was supported by the Korea Science and Engineering Foundation (KOSEF) grant funded by the Korea government (MOST) (No. R01-2005-000-10029-0).

Nomenclature

A-STS : Austenitic stainless steel
PMR : Partially magnetized region
H : Strength of magnetic field [A/m]
STIC : Sheet type induced current
HSA : Hall sensor array
HPF : High-pass-filter
RMS : Root-mean-squared
SSS : Single Hall sensor scanning
DRMS : Distribution of root mean square [V/mm]
D : Depth of the crack [mm]
W : Width of the crack [mm]
L : Length of the crack [mm]
Jt : Density of the induced current on the subsurface [A/m^2]
t : Thickness [mm]
δ : Skin depth [mm]
f : Frequency [Hz]
μ : Permeability [H/m]
σ : Electrical conductivity [A/V]
$\partial D/\partial x$: The differential RMS of Hall voltage to the STIC direction [V/mm]
Diameter[$\partial D/\partial x$] : The interval between the maximum position and the minimum position [mm]
Distance[$\partial D/\partial x$] : The distance between each set of maximum positions [mm]
Max[$\partial D/\partial x$] : The average of the maximum values of $\partial D/\partial x$ [V/mm]
S : The section area of the crack [mm^2]
V : The volume of the crack [mm^3]

Subscripts

C : Crack
EXT : External
S : Critical saturation
HIGH : High spatial resolution by using single Hall sensor scanning
LOW : Low spatial resolution by using the Hall sensor array

Superscripts

′ : Calculated by S_C divide L_C

References

[1] U. G. Goranson, Damage tolerance facts and fiction, *17th Symposium of the International Committee on Aeronautical Fatigue*, Stockholm, Sweden, 1 (1993) 2-105.
[2] D. Y. Hwang, Damage tolerance design and prediction of fatigue life in aircraft structure, *KSME Int. Journal*, 35 (1995) 468-480.
[3] J. Y. Lee, J. S. Hwang and T. Shoji, Numerical Analysis of Magneto-Optical Eddy Current Imaging Using FEM, *Key Engineering Materials*, Korea, 306-308 (2006) 235-240.
[4] D. K. Thome, G. L. Fitzpatrick, R. L. Skaugset and W. C. L. Shih, Aircraft Corrosion and Crack Inspection Using Advanced Magneto-Optic Imaging Technology, *The International Society for Optical Engineering- SPIE Proceedings,* 2945 (1996) 365-373.
[5] G. L. Fitzpatrick, D. K. Thome, R. L. Skaugset and W. C. L. Shih, Magneto-Optic/Eddy Current Imaging of Subsurface Corrosion and Fatigue Cracks in Aging Aircraft, *Review of Progress in Quantitative Nondestructive Evaluation, edited by D.O. Thompson and D.E. Chimenti, Plenum Press*, New York, USA, 15A (1996) 1159-1166.
[6] J. Y. Lee, W. H. Choi, M. S. Kim, D. J. Kim and M. P. Kang, US patents 6,683,452 B2. (2004).
[7] J. Y. Lee and J. S. Hwang, The Detection Probability Improvement of the Far-side Crack on the High Lift-off Using the magnetic Camera, *International Journal of Modern Physics B*, 20 (25-27) (2006) 4631-4636.
[8] J. Y. Lee and J. S. Hwang, The QNDE Using Image Processing of the Magnetic Camera, *International Journal of Modern Physics B*, 20 (25-27) (2006) 4625-4630.
[9] J. Y. Lee, J. S. Hwang, S. H. Choi and J. K. Lim, Detection Probability Improvement for Nondestructive Evaluation Using a Magnetic Camera, *Key Engineering Materials*, Korea, 306-308 (2006) 241-

246.

[10] J. W. Jun, J. S. Hwang, K. J. Kim, K. Ogawa and J. Y. Lee, Development of Signal Processing Circuit of a Magnetic Camera for the NDT of a Paramagnetic Material, *Key Engineering Materials*, Switzerland, 353-358 (2007) 2379-2382.

[11] H. Fukuoka, et al, Nondestructive Evaluation, *Journal of the Japanese Society for Non-destructive Inspection*, Tokyo, Japan (1998) 78.

[12] J. Panaitov, H. J. Krause and Y. Zhang, Pulsed eddy current transient technique with HTS SQUID magnetometer for non-destructive evaluation, *Physics C*, 372-376 (2002) 278-281.

[13] Oxygen-free copper—Manual 2007 CAT.NO. CE100A (Japan : HITACHI).